

The Drivers of Cosmic Dust Temperature Evolution

M. Parente^{1,2,*}, F. Salvestrini^{2,3,**}, G. L. Granato^{2,3,4}, D. Narayanan^{1,5},
R. Tripodi^{6,7,3}, S. Bianchi⁸, M. Bischetti^{2,3,9}, C. Feruglio^{2,3}, F. Fiore^{2,3}, and L. Silva^{2,3}

¹ Department of Astronomy, University of Florida, 211 Bryant Space Sciences Center, Gainesville, FL 32611, USA

² INAF, Osservatorio Astronomico di Trieste, via Tiepolo 11, I-34131, Trieste, Italy

³ IFPU, Institute for Fundamental Physics of the Universe, Via Beirut 2, 34014 Trieste, Italy

⁴ IATE - Instituto de Astronomía Teórica y Experimental, Consejo Nacional de Investigaciones Científicas y Técnicas de la República Argentina (CONICET), Universidad Nacional de Córdoba, Laprida 854, X5000BGR, Córdoba, Argentina

⁵ Cosmic Dawn Center at the Niels Bohr Institute, University of Copenhagen and DTU-Space, Technical University of Denmark

⁶ INAF - Osservatorio Astronomico di Roma, Via Frascati 33, I-00078 Monte Porzio Catone, Italy

⁷ University of Ljubljana FMF, Jadranska 19, 1000 Ljubljana, Slovenia

⁸ INAF-Osservatorio Astrofisico di Arcetri, Largo E. Fermi 5, I-50125 Florence, Italy

⁹ Dipartimento di Fisica “Enrico Fermi”, Università di Pisa, Largo Bruno Pontecorvo 3, Pisa I-56127, Italy

Received September 15, 1996; accepted March 16, 1997

ABSTRACT

Context. Observations of the rest-frame far-infrared (far-IR) emission of galaxies suggest a mild increase of dust temperature T_{dust} with redshift, although constraining T_{dust} in high-redshift systems remains challenging due to limited sampling of the far-IR spectral energy distribution (SED).

Aims. We present and discuss the redshift evolution of T_{dust} predicted by a cosmological galaxy evolution simulation with dust treatment, and interpret its dependence on other galaxy physical properties.

Methods. We use a semi-analytic model of galaxy formation that includes an explicit treatment of dust, post-processed with radiative transfer. Dust temperatures are derived by applying modified blackbody SED fitting to the simulated galaxies, mirroring the methodology adopted in most observational studies.

Results. The dust temperature of simulated galaxies increases with redshift, in broad agreement with observational results. A feature-importance analysis reveals that the star formation rate surface density Σ_{SFR} and the dust-to-gas ratio (DTG) are the main drivers of dust temperature, tracing the intensity of the interstellar radiation field and the optical depth of warm molecular clouds, respectively. Galaxies with higher star formation rate surface density and lower DTGs – common conditions at high- z – are associated with warmer dust. We provide a simple relation to estimate DTG from Σ_{SFR} , T_{dust} , and redshift. Variations in dust grain size and chemical composition have a negligible impact on T_{dust} . Our results are particularly relevant to the study of dust properties with observations of high- z galaxies, where far-IR dust emission is not fully sampled.

Key words. dust – galaxies: evolution – galaxies: high-redshift – submillimetre: galaxies

1. Introduction

Among the various components that contribute to the baryonic mass of the Universe, dust represents an almost negligible fraction of the interstellar medium (ISM; e.g., Galliano et al. 2018), specifically less than 1%. Nevertheless, it plays a fundamental role in a wide range of physical processes: it acts as a catalyst for molecular hydrogen formation (e.g., Wakelam et al. 2017), depletes metals from the gas phase of the ISM (e.g., Jenkins 2009), and absorbs ultraviolet (UV) photons by stars and re-emits them in the infrared (IR) band (e.g. Draine & Lee 1984; Silva et al. 1998; Narayanan et al. 2018). Indeed, dust emission has been detected from the IR to radio wavelengths in galaxies out to very high redshift (e.g., Bakx et al. 2025) thanks to sensitive observations with both ground-based facilities such as the Atacama Large Millimeter Array (ALMA) or the Northern Extended Millimeter Array (NOEMA), and space telescope such as *Herschel*. As a result, dust has become a key tracer for inferring the physical properties of galaxies, such

as star formation activity, gas content, and metal enrichment, and therefore plays a central role in studies of galaxy evolution (Santini et al. 2014; Genzel et al. 2015; Scoville et al. 2016; Algera et al. 2023; Traina et al. 2024a,b; Sun et al. 2025).

The two key dust properties that observations aim to constrain are the dust mass and temperature. The latter provides insight into fundamental physical properties of galaxies – such as the intensity of the radiation field and the spatial distribution of stars relative to dust (Silva et al. 1998). However, determining the temperature of dust grains within a galaxy is a challenging task, as it requires observations over a wide range of wavelengths, from a few tens of microns up to a few millimeters. Furthermore, determining the temperature is degenerate with the dust mass and the dust emissivity index, since the total IR luminosity scales as $L_{\text{IR}} \propto M_{\text{dust}} T_{\text{dust}}^{4+\beta_d}$, where β_d is the emissivity index (e.g., Ferrara et al. 2022). Accurately determining the dust temperature is therefore crucial both for gaining physical understanding of the conditions of the ISM and for deriving robust estimates of the dust mass.

Over the decades, studies of dust temperature have been conducted for both star forming galaxies and AGN, generally

* e-mail: parente.m@ufl.edu

** e-mail: francesco.salvestrini@inaf.it

revealing similar trends and evolutionary behaviors (e.g., Witstok et al. 2023; Tripodi et al. 2024). In many cases, however, the two populations are treated similarly, even though AGN are expected to contribute directly to dust heating even at kiloparsec scales (e.g., Tsukui et al. 2023; Fernández Aranda et al. 2025). This reflects the intrinsic complexity of measuring dust temperatures, which requires broad multi-wavelength coverage and whose reliability strongly depends on the availability and spectral sampling of the photometric data. Some studies have adopted multi-temperature fitting functions and composite models (e.g., Dunne & Eales 2001; Casey 2012; Dale et al. 2012; Kirkpatrick et al. 2015), while others developed empirical templates of the spectral energy distribution (SED) based on distributions of interstellar radiation field intensities heating the dust grains (e.g., Draine & Li 2007; Galliano 2018). However, these approaches are characterized by a large number of free parameters and are therefore difficult to apply to large samples of galaxies, especially at high redshift ($z > 2$), where only sparse dust continuum detections are often available. In such cases, fitting the dust SED with a single-temperature modified blackbody (MBB) represents a reasonable and widely adopted approximation (e.g., Hildebrand 1983; Magnelli et al. 2012; Simpson et al. 2017; Carniani et al. 2019; Bakx et al. 2021; Witstok et al. 2023; Tripodi et al. 2024).

Regardless of the method employed or the quality of the SED sampling, it is important to recognize that most observational analyses assume a single, isothermal dust temperature. In reality, galaxies contain broad, multi-temperature dust distributions arising from the combination of diffuse ISM and compact star forming regions (Draine 2003). Consequently, the commonly adopted single-temperature approximation can bias dust mass estimates (Sommovigo & Algera 2025). Dust temperature measurements obtained in this way should therefore be regarded as effective, model-dependent parameters rather than direct physical temperatures.

Taken together, current observational studies suggest that the average effective dust temperature of star forming galaxies increases with redshift. Measurements spanning from the local Universe to early cosmic times – based on both individual detections and stacked samples – point to a systematic, albeit modest, rise in dust temperature (e.g., Schreiber et al. 2018; Viero et al. 2022; Witstok et al. 2023), while the inferred dust temperature distribution at redshift $z > 1$ remains extremely broad. However, observations at high z are subject to strong selection effects, as only the most massive, intensely star forming, and dust-rich systems are typically detected (e.g., Lim et al. 2020). Consequently, the detailed form of the temperature–redshift relation is still poorly constrained and depends sensitively on sample selection, analysis techniques, and assumptions regarding dust physics.

From a theoretical perspective, numerous studies have aimed to predict dust temperatures in galaxies using a variety of approaches. The most widely adopted and physically motivated method involves post-processing galaxy formation simulations with radiative transfer (RT) codes (e.g., SKIRT; Camps & Baes 2015) to model dust heating, temperature distributions, and the resulting IR emission (e.g. Behrens et al. 2018; Aoyama et al. 2019; Liang et al. 2019; Ma et al. 2019; Pallottini et al. 2022; Vijayan et al. 2022; Shen et al. 2022). While these studies differ substantially in their modeling strategies and in how dust temperature is defined, they broadly agree on a mild increase of dust temperature with redshift, primarily driven by higher specific star formation rates (SFRs) and SFR surface densities. It is nevertheless important to note that, despite growing efforts within the numerical extragalactic community to explicitly

model dust in galaxy evolution simulations (e.g., Parente 2025), the majority of the works above do not include such treatments and instead assume a fixed dust-to-metal ratio to link dust to the metal content (but see Granato et al. 2021; Lower et al. 2024). In parallel, a number of simple yet physically motivated analytic models have been developed to address this problem. For instance, Sommovigo et al. (2022b) associates the higher dust temperatures observed at high redshift to shorter gas depletion times driven by more intense cosmological accretion at early epochs, while Hirashita & Chiang (2022) attributes elevated T_{dust} at high z to the combined effects of low dust-to-gas (DTG) ratios and enhanced star formation activity.

In this work, we build a theoretical framework to investigate the evolution of dust temperature with redshift in star forming galaxies by combining all the key ingredients required for this purpose. Specifically, we employ: (i) a cosmological galaxy evolution simulation with explicit dust modeling (Parente et al. 2023); (ii) explicit RT calculations to model dust emission (Silva et al. 1998); and (iii) an observationally motivated dust temperature determination obtained by fitting the SEDs derived from our simulations (Tripodi et al. 2024). We present predictions for the redshift evolution of T_{dust} , which we compare against an extensive compilation of observational measurements in several samples of galaxies and AGN from the local Universe up to $z \sim 8$, and we further explore its dependence on key galaxy properties, most notably the SFR surface density and the DTG ratio.

The paper is organized as follows: the results of the simulation used in this work are presented in Sect. 2, including our analysis to derive the estimates of T_{dust} . Sect. 3 presents the analysis results, compares them with literature findings, and provides a physical interpretation of our modeled T_{dust} and its dependence on key galaxy properties. Finally, the results are summarized in Sect. 4.

2. Simulation catalog

Our catalog of simulated galaxies is built using the L-GALAXIES semi-analytic model (SAM), adopting its latest public release (Henriques et al. 2020)¹ together with the updates presented in Parente et al. (2023). Among these updates, particularly relevant for this work is the implementation of a new model for the formation and evolution of dust grains, inspired by the dust prescriptions previously developed for hydrodynamical simulations (Granato et al. 2021; Parente et al. 2022).

The dust model (for a detailed description, see Sect. 2.1 of Parente et al. 2023) includes two grain sizes (small and large, with radii of 0.005 and 0.05 μm respectively) and two chemical compositions (carbonaceous and silicate). Dust grains are produced in the envelopes of AGB stars and in the ejecta of core-collapse supernovae, and are subsequently released into the ISM. Their mass and size evolution is regulated by several processes, including accretion, destruction in supernova shocks, thermal sputtering, shattering, and coagulation. The resulting dust masses and grain properties are a key ingredient for predicting the SED of galaxies.

The SAM is run on the MILLENNIUM merger trees (Springel et al. 2005; 500 Mpc/h box size), rescaled to a Planck cos-

¹ The source code is available at https://github.com/LGalaxiesPublicRelease/LGalaxies_PublicRepository/releases/tag/Henriques2020

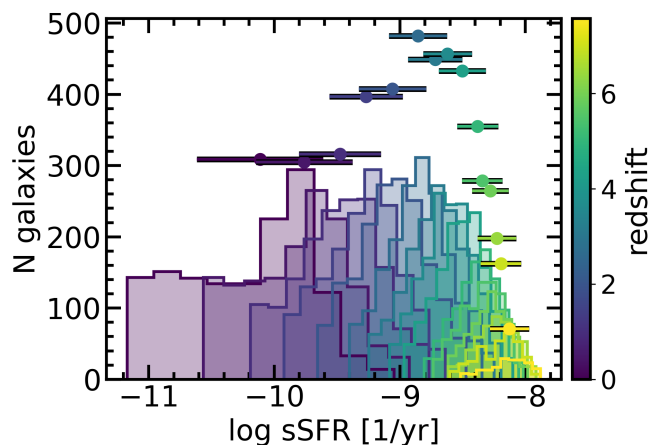


Fig. 1: Distribution of the specific SFR of the simulated galaxies used in the analysis across different redshifts (see colorbar). Circles and horizontal bars indicate the median and standard deviation of the distribution at each redshift.

mology² (Planck Collaboration et al. 2014) with $h = 0.673$, $\Omega_m = 0.315$, $\Omega_b = 0.0487$, and $\sigma_8 = 0.829$. A Chabrier (2003) IMF is adopted. In our analysis we consider galaxies with $\log(M_{\text{stars}}/M_\odot) \geq 9$, close to the resolution limit of the underlying dark matter simulation (e.g. Guo et al. 2011). Passive galaxies are excluded, defined as those with specific SFR (sSFR) more than 1.5σ below the median³ at each redshift. To reduce computational cost, we post-process a representative subsample of galaxies per redshift with radiative transfer, uniformly sampling the full stellar-mass range. This results in $\approx 2,500$ galaxies at $z = 0.0$ and ≈ 250 galaxies at $z = 7.57$. The sSFR distribution of our simulated galaxy sample is shown in Fig. 1.

2.1. Simulated SEDs with radiative transfer

In order to obtain the SED of our simulated galaxies, we exploit the radiative transfer code GRASIL (Silva et al. 1998; Granato et al. 2000), which models stellar emission and its interaction with dust, including absorption and thermal re-emission. GRASIL uses the star formation histories, galaxy geometry, and dust masses and properties as predicted by the SAM. While briefly summarize its strategy in the following, we refer to Parente et al. (2025) for a description of the coupling between this RT pipeline and the SAM.

Galaxies are modeled with a disk-like ISM and a stellar component composed of a disc and a bulge. Stellar and ISM discs follow exponential radial and vertical profiles, with scale lengths provided by the SAM, while the bulge follows a King profile. Stellar emission is computed by convolving the disc and bulge star formation histories with simple stellar population models. RT accounts for the interaction between starlight and dust grains, whose abundances, compositions, and sizes are predicted by the SAM. Dust is distributed between molecular clouds and a diffuse ISM, with the molecular fraction provided by the SAM. Stars are assumed to form in molecular clouds and escape on a characteristic timescale $t_{\text{esc}} = 3$ Myr, after which their radiation propagates in the diffuse medium. Full RT calculations are performed

² The original MILLENNIUM cosmology is rescaled following Angulo & White (2010); Angulo & Hilbert (2015).

³ The median is calculated using galaxies with $M_{\text{stars}} < 10^{10} M_\odot$ to avoid bias from massive quiescent systems.

within molecular clouds, while a simplified treatment is adopted for the diffuse phase. The resulting stellar and dust emission is combined to produce galaxy SEDs spanning $0.1 - 10^4 \mu\text{m}$.

2.2. SED binning

Given the SED obtained from the RT post-processing described in Sect. 2.1 for galaxies spanning the redshift range $0 \lesssim z \lesssim 7.5$, we extracted flux densities from the model SED over the rest-frame wavelength interval $40 \mu\text{m} - 3 \text{ mm}$. To mimic realistic observations, we selected the flux corresponding to the wavelength closest to the effective wavelength of representative bands in the far-IR regime. Specifically, we considered the 100 and 160 μm bands from the Photodetector Array Camera and Spectrometer (PACS) and the 250 μm band from the Spectral and Photometric Imaging Receiver (SPIRE), both onboard the *Herschel* satellite. In addition, we included ALMA bands covering observed-frame wavelengths from 3.5 mm to 0.35 mm, corresponding to Bands 2 and 10⁴, respectively. We excluded the *Herschel*/SPIRE 350 and 500 μm bands, as they overlap with ALMA Bands 10 and 9, respectively. This procedure yielded a set of 8 or 9 photometric points for each SED, depending on the galaxy redshift, sampling both sides of the peak of the far-IR emission as well as the Rayleigh–Jeans regime. The full list of representative wavelengths adopted for each redshift bin is provided in Table 1.

Table 1: Photometric bands adopted in the SED fitting.

z	Bands
0.05	PACS100, PACS160, SPIRE250, 10, 9, 8, 7, 6, 5
0.51	PACS160, SPIRE250, 10, 9, 8, 7, 6, 5, 4
1.04	PACS160, SPIRE250, 10, 9, 8, 7, 6, 5, 4
1.48	PACS160, SPIRE250, 10, 9, 8, 7, 6, 5, 4
2.07	SPIRE250, 10, 9, 8, 7, 6, 5, 4, 3
2.64	SPIRE250, 10, 9, 8, 7, 6, 5, 4, 3
3.11	SPIRE250, 10, 9, 8, 7, 6, 5, 4, 3
3.65	SPIRE250, 10, 9, 8, 7, 6, 5, 4, 3
4.28	10, 9, 8, 7, 6, 5, 4, 3
5.03	10, 9, 8, 7, 6, 5, 4, 3
5.46	10, 9, 8, 7, 6, 5, 4, 3
5.92	10, 9, 8, 7, 6, 5, 4, 3
6.42	10, 9, 8, 7, 6, 5, 4, 3, 2
6.97	10, 9, 8, 7, 6, 5, 4, 3, 2
7.57	10, 9, 8, 7, 6, 5, 4, 3, 2

Note: Redshift bins and the corresponding photometric bands used to bin each galaxy SED, listed in increasing wavelength order. PACS and SPIRE stand for *Herschel* PACS and SPIRE instruments; the numbers between 2 and 10 indicate the corresponding ALMA bands.

2.3. Fit of the far-IR SED

To fit the mock photometric points of the SEDs we used the publicly available EOS-DUSTFIT code⁵. In EOS-DUSTFIT, the cold dust continuum emission is modeled with a single-temperature modified black body (MBB) function, assuming an optically thin

⁴ <https://www.eso.org/public/italy/teles-instr/alma/receiver-bands/>

⁵ EOS-DUSTFIT is a publicly available tool for fitting the cold dust SED of galaxies (<https://github.com/roberta96/EOS-Dustfit>). Details about the modeling can be found on the GitHub page and in Tripodi et al. (2024); Salvestrini et al. (2025).

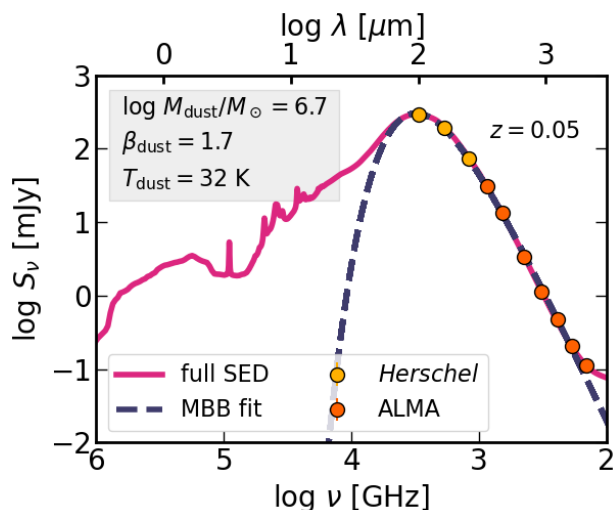


Fig. 2: Example of the SED fitting procedure for a single model galaxy at $z = 0.05$. The full SED from our model is shown in red, while the binned points – representing mock *Herschel* and ALMA observations – are plotted as symbols. The dashed line shows the resulting MBB fit to these points, with the fitted parameters reported in the top-left corner.

regime, given by:

$$S_{\nu}^{\text{obs}} = \frac{S_{\nu/(1+z)}^{\text{obs}}}{1+z} = \frac{\Omega}{(1+z)^3} [B_{\nu}(T_{\text{dust}}(z)) - B_{\nu}(T_{\text{CMB}}(z))] (1 - e^{-\tau_{\nu}}), \quad (1)$$

where $\Omega = (1+z)^4 A_{\text{gal}} D_L^{-2}$ is the solid angle, and A_{gal} and D_L are the projected surface area and the luminosity distance of the galaxy, respectively. The dust optical depth is defined as

$$\tau_{\nu} = \frac{M_{\text{dust}}}{A_{\text{gal}}} k_0 \left(\frac{\nu}{250 \text{ GHz}} \right)^{\beta_{\text{dust}}}, \quad (2)$$

where β_{dust} is the dust emissivity index and $k_0 = 0.45 \text{ cm}^2 \text{ g}^{-1}$ is the mass absorption coefficient (Beelen et al. 2006). The effect of the cosmic microwave background (CMB) on the dust temperature is accounted for through

$$T_{\text{dust}}(z) = \left[(T_{\text{dust}})^{4+\beta_{\text{dust}}} + T_0^{4+\beta_{\text{dust}}} \left((1+z)^{4+\beta_{\text{dust}}} - 1 \right) \right]^{1/(4+\beta_{\text{dust}})}, \quad (3)$$

where $T_0 = 2.73 \text{ K}$. The model also includes the contribution of the CMB emission, described by the Planck function $B_{\nu}(T_{\text{CMB}}(z)) = B_{\nu}(T_0(1+z))$ (da Cunha et al. 2013).

The solid angle Ω is estimated assuming that the size of the emitting region is 1.5 times the scale radius obtained from fitting the radial profile of the cold gas with an exponential function⁶. This region encompasses nearly 90% of the dust in the simulated galaxy, which should roughly match the bulk of the dust-continuum emission that is usually collected with submillimeter observations, especially at high redshift (e.g., Hodge et al. 2016; Gullberg et al. 2019). In our analysis, we left three parameters in the MBB model free to vary, namely

⁶ We tested how sensitive our results are to the assumed source size by doubling and halving the radius. The three best-fitting parameters remain consistent with our baseline results within the uncertainties. For instance, doubling the size lowers the median T_{dust} by at most $\approx 2 \text{ K}$.

dust temperature (T_{dust}), dust mass (M_{dust}), and the emissivity index (β_{dust}). A conservative 10% uncertainty was adopted to account for calibration inaccuracies inherent to observations. EOS-DUSTFIT explores the parameter space for each SED using a Markov chain Monte Carlo algorithm implemented in the *emcee* package (Foreman-Mackey et al. 2013). A uniform distribution for priors is assumed for fitting parameters in the range $5 \leq T_{\text{dust}}/\text{K} \leq 300$, $5 \leq \log(M_{\text{dust}}/M_{\odot}) \leq 9$, and $0.5 \leq \beta_{\text{dust}} \leq 3.0$. We ran 30 chains, each with 500 trials and a burn-in phase of 200 steps, for a total of 15,000 steps per galaxy. We adopted the 50th percentile of the posterior distribution as the best-fit value, while the errors are calculated considering the 16th and 84th percentiles. The results of the SED fitting are presented in Sect. 3, while Fig. 2 provides an explicit example of the procedure for a model galaxy at $z = 0.05$.

3. Results

3.1. Redshift evolution of T_{dust}

We present the redshift evolution of the dust temperature, T_{dust} , in Fig. 3, comparing our results with a compilation of measurements from the literature. All data points and trends shown in the figure are based on observational studies, with the sole exception of the relation from Liang et al. (2019) and Sommovigo et al. (2022b), which represent theoretical predictions.

For each redshift bin, we report the median value and 16 – 84th dispersion of the T_{dust} measurements for the simulated galaxy population. Our results exhibit a clear redshift evolution of T_{dust} , increasing from $\approx 20 \text{ K}$ in the local Universe up to $\approx 70 \text{ K}$ at $z \approx 7.5$. This trend is in good agreement with the behaviour inferred from previous results in the literature. Using the *polyfit*⁷ routine from the Python *numpy* package, we perform a linear fit, finding:

$$T_{\text{dust}} = (6.95 \pm 0.68) \times z + (25.2 \pm 1.6). \quad (4)$$

We note that the dispersion of the T_{dust} measurements increases with redshift, from $\approx 2 \text{ K}$ in the local Universe to $\approx 15 \text{ K}$ – roughly 20% of the temperature in the highest redshift bin. The increase of the T_{dust} dispersion with redshift is briefly discussed in light of the temperature dependence on SFR surface density and DTG in Sect. 3.3.

3.1.1. Comparison with observations

The results of our analysis are broadly consistent with the observational-based results from the literature⁸.

In the nearby Universe, our analysis predicts a T_{dust} which is close to that derived for the local star forming galaxies (SFGs), as those analyzed in the JINGLE survey (Lamperti et al. 2019) and in Sommovigo et al. (2021). On the contrary, the median value of T_{dust} measured in the HERUS sample (Clements et al.

⁷ <https://numpy.org/doc/stable/reference/generated/numpy.polyfit.html>

⁸ We remind that we compiled observational results obtained using methodologies broadly similar to those adopted in our analysis. Whenever possible, we verified the consistency among the different approaches, finding overall good agreement. For the sake of brevity, we limit the discussion here to a direct comparison with the results available in the literature. Additional details on the methodologies employed and on the specific assumptions adopted in each study are summarized in App. A. We also refer the reader to the original references cited throughout the text for a comprehensive description.

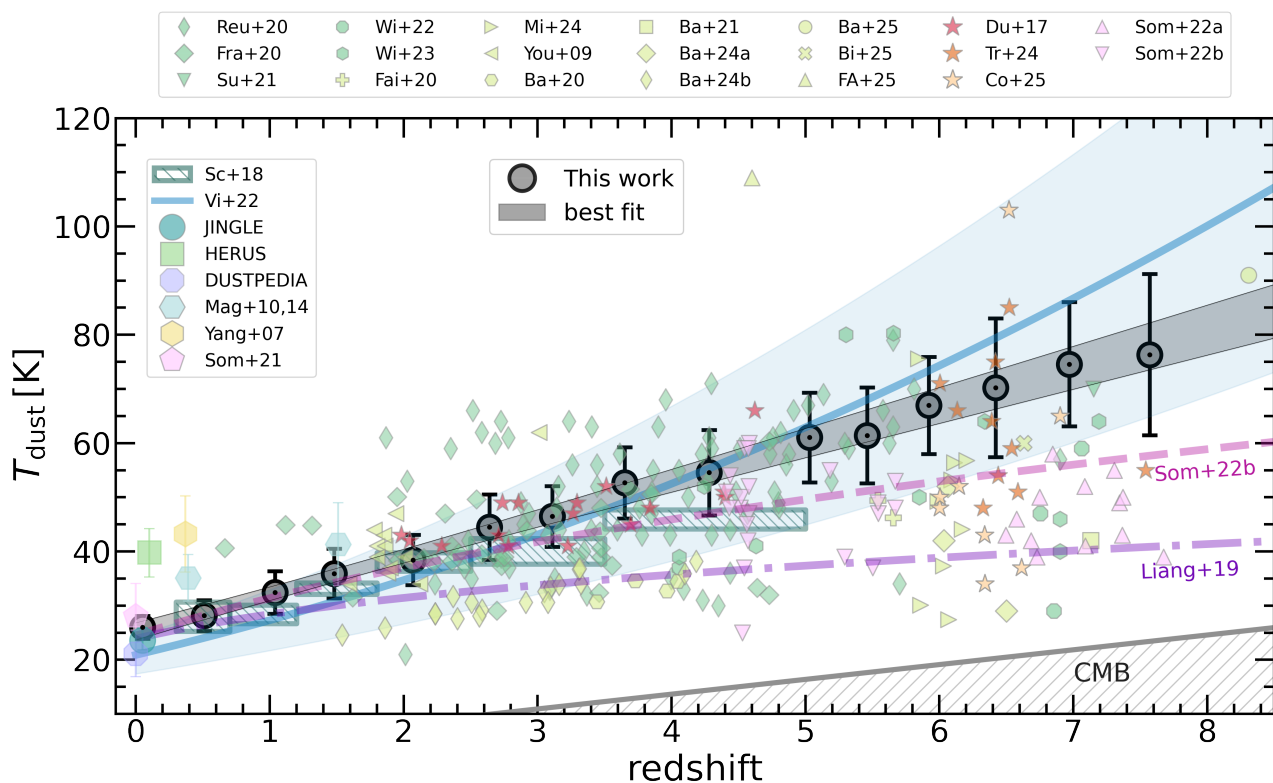


Fig. 3: Dust temperature evolution with redshift. Our results from simulated galaxies are shown as grey circles (median values), with error bars indicating the 16–84th percentile dispersion. A linear fit to our results is displayed as a shaded grey region (Eq. 4). Measurements from the literature are also included for comparison (see extensive description in App. A). Owing to the relatively limited redshift range of some samples, which would make the distribution of individual objects difficult to visualize, we report the median T_{dust} values and their standard deviations (HERUS from Clements et al. 2018; JINGLE from Lamperti et al. 2019; DustPedia from Nersesian et al. 2019; Magdis et al. 2010, 2014; Yang et al. 2007; Sommovigo et al. 2021). Large samples extending to $z > 2$ are those presented by Schreiber et al. (2018) and Viero et al. (2022) (Sc+18 and Vi+22, respectively). Less populated datasets – shown as individual galaxies – are also included: Reuter et al. (2020); Franco et al. (2020); Sugahara et al. (2021); Witstok et al. (2022, 2023); Faisst et al. (2020); Mitsuhashi et al. (2024); Younger et al. (2009); Bakx et al. (2020a, 2021, 2024a,b, 2025); Bing et al. (2025); Sommovigo et al. (2022a,b). We also include observational samples of high-redshift AGN and QSOs (Duras et al. 2017; Bischetti et al. 2021; Tripodi et al. 2024; Costa et al. 2025; Fernández Aranda et al. 2025). Theoretical predictions from the physical model of Sommovigo et al. (2022b) and the numerical simulations of Liang et al. (2019) are shown as shaded lines. For reference, the CMB temperature is indicated by a hatched region.

2018), which includes local ultra-luminous infrared galaxies (ULIRGs), is roughly 3σ higher than our predictions. A similar behavior is also observed for samples of ULIRGs at $z < 1$, such as those presented by Yang et al. (2007) and Magdis et al. (2014). The relatively high T_{dust} value measured in ULIRGs when compared to normal SFGs is likely driven by the intense and concentrated star formation activity (SFR is up to a few hundreds $M_{\odot}\text{yr}^{-1}$; e.g., Magdis et al. 2010; Hogan et al. 2022) in this class of dusty objects.

The same duality in the behaviour of SFGs and ULIRGs is present when moving at intermediate redshifts ($1 \lesssim z \lesssim 4$), with our results closely following the empirical trends reported in the literature (Schreiber et al. 2018; Viero et al. 2022), and within the observed scatter defined by samples presented by Younger et al. (2009) and Franco et al. (2020). Even luminous quasars (QSOs) with accurate treatment of the reprocessing of the AGN emission, such as the WISSH sample by Duras et al. (2017), strictly

follow our prediction of the evolution of T_{dust} with redshift.

At higher redshift ($z \gtrsim 5$), the observational data display a large dispersion, reflecting both intrinsic diversity among galaxies and increasing uncertainties due to limited photometric coverage. In this regime, our simulated galaxies populate the upper part of the observed T_{dust} distribution and are consistent with measurements for luminous systems such as those in the ALPINE, REBELS (e.g., Sommovigo et al. 2022a,b; see also Algera et al. 2024a,b, 2025) samples, as well as the objects from Witstok et al. (2023) and Tripodi et al. (2024). Regarding Tripodi et al. (2024), the authors adopted a different parametrization for the evolution of T_{dust} with redshift (see their Eq. 6). Nevertheless, the trends derived from both their full galaxy sample and their QSO-only sample are consistent with ours within the respective uncertainties.

We remind the reader that, to make the different observational samples easier to compare, we chose literature works that

adopted broadly similar methodologies to measure T_{dust} (see App. A). The heterogeneous galaxy selection criteria and the sparse sampling of the far-IR emission adopted in the studies shown in Fig. 3, particularly at $z > 1$, likely contribute significantly to the observed dispersion. Indeed, the spread in T_{dust} reaches up to ≈ 20 K at Cosmic Noon ($1.5 < z < 4.5$), even among galaxies within the same sample (e.g., Reuter et al. 2020). This scatter likely arises from a combination of large measurement uncertainties (with $\Delta T_{\text{dust}}/T_{\text{dust}}$ reaching up to $\approx 30\text{--}40\%$) and differences in sample selection. Notably, when comparing with larger samples such as that presented in Viero et al. (2022), the observed dispersion is found to increase with redshift, in agreement with our results.

Finally, we note that the observational samples considered also include galaxies hosting AGN and QSOs, whose contributions are not modeled in our simulation. Furthermore, even if most of the ULIRGs included here were selected to be dominated by star formation activity (see Magdis et al. 2014), it is difficult to rule out any potential contamination from dust-obscured AGN activity obscured by the total far-IR emission. Therefore, determining the actual impact of AGN activity on dust heating, even on kiloparsec scales, is far from trivial. Growing evidence indicates that AGN can contribute up to $\approx 50\%$ of the total far-IR emission (e.g., Tsukui et al. 2023), with a pronounced spatial gradient in the peak dust temperature (e.g., Fernández Aranda et al. 2025). However, the substantial scatter characterizing the T_{dust} distribution, including that of high-redshift AGNs shown in Fig. 3, suggests that the intensity of the AGN-powered ionizing radiation field in the galaxy center is not the only driving mechanism to contribute to dust heating (see the discussion in Sect. 3.3).

3.1.2. Comparison with theoretical models

For the comparison with theoretical predictions, we consider the models of Sommovigo et al. (2022b) and Liang et al. (2019). The former is based on an analytic framework that links dust temperature to the cosmological evolution of galaxy properties, in particular to gas depletion times, which are shorter in high-redshift galaxies owing to enhanced cosmological accretion rates (as also confirmed by observations; e.g. Tripodi et al. 2024; Salvestrini et al. 2025). While this model predicts an overall increase of T_{dust} with redshift, in agreement with the above-mentioned observational results up to intermediate redshifts ($z \sim 4$), it yields systematically lower temperatures than those inferred from our analysis and from some observational samples at $z \gtrsim 5$. However, we note that the Sommovigo et al. (2022b) relation presented here is based on their solar metallicity model. The authors point out that variations in column density and metallicity can lead to temperature differences of approximately $\Delta T_{\text{dust}} \approx 25$ K. For instance, their optically thick model with a metallicity of $0.3 Z_{\odot}$ – associated with lower DTG ratios, as expected at high redshift – yields $T_{\text{dust}} \approx 60$ K at $z \approx 6$, in better agreement with our model.

The work⁹ by Liang et al. (2019) instead is based on the analysis of massive galaxies at $z \approx 2\text{--}6$ using hydrodynamic simulations from the FIRE project (Hopkins et al. 2014), coupled with RT calculations performed with SKIRT (Camps & Baes 2015). Al-

⁹ We report their predicted peak temperature, defined as the temperature inferred from the wavelength at which the far-IR emission reaches its maximum. A discussion of the different methods used to estimate dust temperature is presented in the original work, to which we refer the reader.

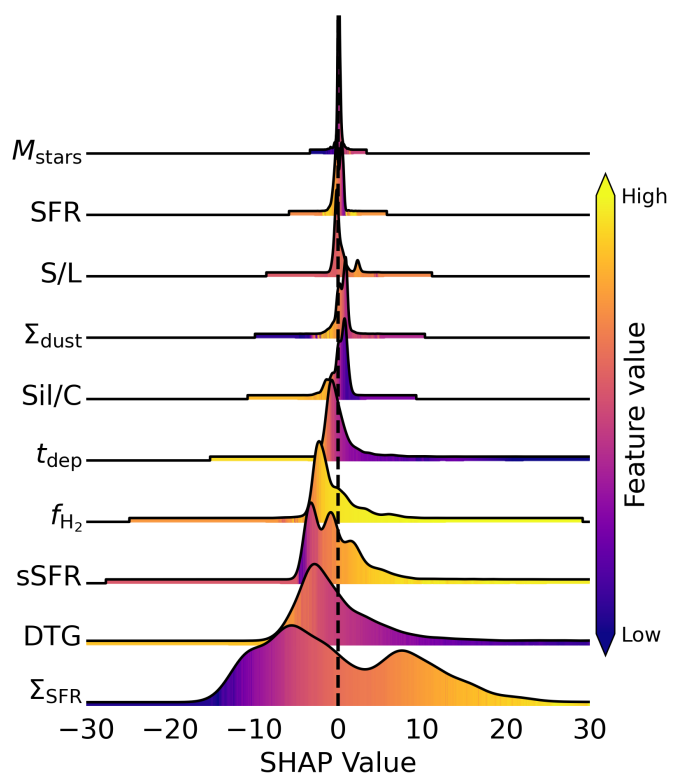


Fig. 4: Ridgeline plot showing the distribution of SHAP values for each feature in predicting T_{dust} in our galaxy sample. The dashed vertical line marks zero. Histogram areas are colored according to the normalized values of each feature, from dark blue (low) to yellow (high).

though their results also show an increase in dust temperature with redshift, the inferred temperatures are systematically lower than ours, with the difference becoming larger at high redshift. While a detailed comparison between their simulations and our semi-analytic framework is beyond the scope of this work, we here highlight two key differences that are likely to drive the aforementioned difference in T_{dust} .

First, unlike our model, the Liang et al. (2019) FIRE simulations do not include an explicit treatment of dust formation and evolution. Dust is therefore assumed to directly trace metals through a fixed dust-to-metals ratio of 0.4. This assumption represents a significant source of uncertainty, particularly at high redshift, where our model predicts dust-to-metals ratios as low as $\approx 10^{-2}$. Second, the FIRE simulations achieve exceptionally high spatial resolution, allowing them to resolve the structure of the ISM. On the contrary, our SAM adopts a simplified geometric description of the ISM, which is modeled as a diffuse disk with embedded spherical molecular clouds. Given the crucial role of geometry in radiative transfer calculations (Silva et al. 1998) and its importance in shaping our results (see the discussion in Sect. 3.2), this difference is likely another major contributor to the discrepancies.

3.2. The driver of the $T_{\text{dust}} - z$ relation

We perform a Shapley analysis (Shapley 1953) to quantify the relative importance of different physical properties of galaxies in determining their dust temperature across redshift. This technique – already adopted in similar problems in astrophysics

Table 2: Feature importance in predicting T_{dust}

Feature	Importance
Σ_{SFR}	7.35
DTG	3.62
sSFR	2.42
f_{H_2}	2.42
t_{dep}	1.11

Note: Feature importances are derived from the Shapley analysis as the mean of absolute values of SHAP values for each feature. Only features with importances larger than 1 are shown.

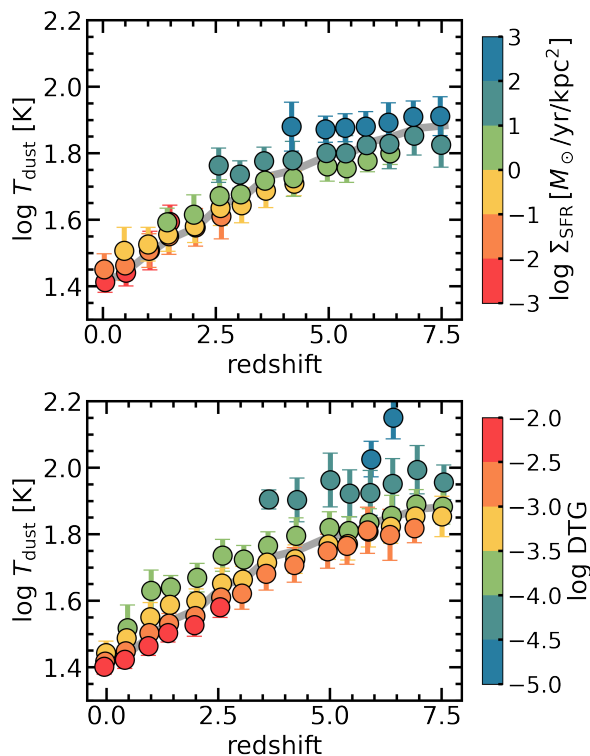


Fig. 5: Dust temperature evolution with redshift separating galaxies in bins of SFR surface density (Σ_{SFR} ; top panel) and dust-to-gas ratio (DTG; bottom panel), as indicated by the colorbar. Each point and errorbar indicates the median and 16–84th percentiles of the distribution. Gray lines in the background refer to the full population.

(e.g., Gilda et al. 2021; Narayanan et al. 2025) – originates from game theory and its original goal was to determine how team members cooperating toward a common goal should divide the resulting prize according to their individual contributions. Essentially, it assigns each feature a Shapley (or SHAP) value, representing the contribution of that feature to the model output. This method not only identifies which features most strongly influence the predictions, but also indicates the direction of their effects. Conceptually, a Shapley value measures how much a given feature shifts the model prediction away from its expected value when that feature is held fixed. Larger absolute SHAP values indicate stronger feature influence, while positive (negative) values correspond to an increase (decrease) in the predicted quantity.

In this work, we use the Shapley analysis to clarify the role

of various galaxy physical properties in driving the dust temperature value, and in particular, its increase with redshift. The considered features (the *players* in Shapley terminology) include the star formation rate (SFR), specific SFR (sSFR = SFR/ M_{stars}), SFR surface density ($\Sigma_{\text{SFR}} = \text{SFR}/A_{\text{gal}}$)¹⁰, gas depletion time ($t_{\text{dep}} = M_{\text{gas}}/\text{SFR}$), stellar mass (M_{stars}), dust mass (M_{dust}), dust surface density ($\Sigma_{\text{dust}} = M_{\text{dust}}/A_{\text{gal}}$), dust-to-gas mass ratio (DTG = $M_{\text{dust}}/M_{\text{gas}}$), molecular gas fraction ($f_{\text{H}_2} = M_{\text{H}_2}/M_{\text{gas}}$), and the mass ratios of small-to-large (S/L) and silicate-to-carbonaceous (Sil/C) grains. These quantities are not only fundamental descriptors of galaxy evolution, but also trace the physical mechanisms that govern dust heating: the intensity of the interstellar radiation field (linked to SFR), the structural geometry of the galaxy (through surface densities), and the abundance and composition of dust.

The first step in performing the Shapley analysis is to construct a model capable of predicting the dust temperature for our galaxy sample. We trained a supervised regression model based on Extreme Gradient Boosting (XGBoost)¹¹, whose goal is to predict the target quantity (in our case T_{dust}) from a set of input features. The sample of galaxies was randomly divided into training and test subsets using an 80/20 split. The model achieves an R^2 score¹² of $\approx 98\%$ on the training set and $\approx 93\%$ on the test set, indicating good predictive accuracy and no significant overfitting. We then applied the SHAP framework¹³ to compute the SHAP values for each feature and interpret the contribution of individual features to the model outputs. The results are illustrated in Fig. 4 as a ridgeline (or joy) plot¹⁴. A quantitative summary of the most influential features is presented in Tab. 2, where the importance of each feature is expressed as the mean of the absolute SHAP values.

The Shapley analysis clearly identifies the SFR surface density as the main feature contributing to the value of the dust temperature: higher (lower) Σ_{SFR} values correspond to higher (lower) T_{dust} , as shown by the colors in Fig. 4. Other relevant features in this analysis are the DTG ratio, sSFR, molecular gas fraction, and depletion time, with galaxies featuring lower DTG, higher star formation activity, and larger molecular gas fractions being associated with warmer dust, respectively.

The role of the two most important features, Σ_{SFR} and DTG, on T_{dust} is further illustrated in Fig. 5, which shows the redshift evolution of dust temperature across different bins of these quantities. A similar analysis for the three other properties listed in Tab. 2 is presented in App. B. The adopted binning scheme highlights that galaxies at higher redshift reach significantly larger star formation surface densities, up to $\gtrsim 10^2 M_{\odot} \text{yr}^{-1} \text{kpc}^{-2}$, and lower DTG ratios, down to $\lesssim 3 \times 10^{-5}$, both of which contribute to higher dust temperatures.

The relevance of Σ_{SFR} stands in its ability to capture two key factors driving dust heating: the intensity of the UV radiation field (traced by the SFR) and the spatial geometry (traced by the size of the galactic disk). More compact star forming galaxies feature

¹⁰ The surface of the galaxy is estimated as πR_{gas}^2 , being R_{gas} the gas scale radius, consistently with what is used in the SED fitting procedure (Sect. 2.3).

¹¹ <https://xgboost.readthedocs.io/en/stable/>

¹² This is a metric indicating the quality of the model performances, with 100% indicating the best possible score (see https://scikit-learn.org/stable/modules/generated/sklearn.metrics.r2_score.html).

¹³ <https://shap.readthedocs.io/en/latest/index.html>

¹⁴ The term *joy plot* is commonly used as a tribute to the *Unknown Pleasures* album cover by Joy Division (1979).

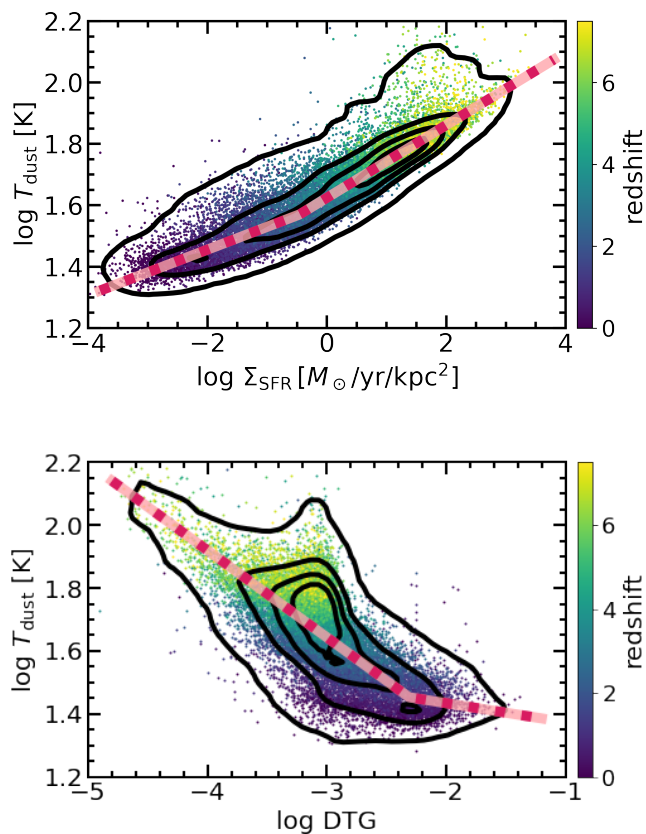


Fig. 6: Dust temperature as a function of Σ_{SFR} and DTG. Each point represents a galaxy and is color coded by redshift, while the black contours correspond to the full sample. The red dashed line shows a broken power law fit to data (Tab. 3).

higher radiation energy densities, leading to more efficient heating of dust grains. This is mostly relevant to diffuse dust, which is distributed throughout the galactic disk.

The relevance of the DTG is twofold. First, galaxies with a lower DTG contain fewer dust grains, which results in more efficient heating for a given SFR. Second, the DTG is relevant for the radiative transfer in dense molecular clouds. These systems are optically thick, often featuring self-absorption of IR photons emitted by dust. The optical depth is determined by DTG (and by the $M_{\text{MC}}/R_{\text{MC}}^2$ ratio, a parameter of the RT model), with lower DTGs corresponding to lower optical depths. In these cases, inner shells of the MCs become more transparent and can thus contribute to IR emission, which is hotter than the diffuse one.

In conclusion, the increase of T_{dust} with redshift is mainly driven by the prevalence, in the early Universe, of galaxies with higher SFR surface densities. A secondary, less dominant effect – according to our Shapley analysis – comes from the enhanced contribution of lower DTGs. We also note that dust properties – namely, size and chemical composition of grains – do not play a relevant role.

3.3. Temperature scaling relations

Figure 6 shows the dependence of galaxy dust temperature on the two properties found to have the strongest impact, namely the SFR surface density and DTG ratio. Analogous relations for the three other influential properties listed in Tab. 2 are presented in

Table 3: Best-fit parameters describing the relation between T_{dust} and various galaxy properties.

x	a	b	x_{crit}	q
Σ_{SFR}	0.070	0.11	-0.63	1.6
DTG	-0.28	-0.060	-2.3	0.81
sSFR	0.096	0.30	-9.3	2.4
f_{H_2}	0.22	0.96	-0.39	1.6
t_{dep}	-0.26	-0.033	0.80	1.6

Notes: The fit relations are broken power laws (Eq. 5) where $y = \log T_{\text{dust}}[\text{K}]$ and $x = \log \Sigma_{\text{SFR}}[M_{\odot}/\text{yr}/\text{kpc}^2]$, $\log \text{DTG}$, $\log \text{sSFR}[\text{yr}^{-1}]$, $\log f_{\text{H}_2}$, or $\log t_{\text{dep}}[\text{Gyr}]$.

App. B. Dust temperature increases systematically with increasing Σ_{SFR} and with decreasing DTG. To provide a convenient, ready-to-use parametrization of these trends, we fit the relations with a broken power law of the type

$$y(x) = \begin{cases} a x + q, & x < x_{\text{crit}} \\ b(x - x_{\text{crit}}) + (a x_{\text{crit}} + q), & x \geq x_{\text{crit}}. \end{cases} \quad (5)$$

We adopt the broken power-law model rather than a simple linear fit to account for the flattening of the relation at low redshifts. The best-fit coefficients – both for this relation and for those shown in Fig. B.2 – are listed in Table 3.

As indicated by the critical values of the broken power-law fits, both relations show a flattening at $z \lesssim 2$, occurring for relatively high DTG ratios ($\gtrsim 5 \cdot 10^{-3}$) and low Σ_{SFR} ($\lesssim 0.1 M_{\odot} \text{ yr}^{-1} \text{ kpc}^{-2}$). The steeper slopes observed at higher redshifts could partially explain the evolution of the T_{dust} scatter discussed in Sect. 3.1: at high z , even small variations in DTG or Σ_{SFR} produce significant changes in T_{dust} , whereas at low z the relation flattens.

Given the clear dependence of the dust temperature on Σ_{SFR} and DTG, we use our results to provide a relation that allows estimation of the DTG from Σ_{SFR} , T_{dust} , and redshift. This is particularly useful for observational studies, where Σ_{SFR} and T_{dust} are typically derived from SED fitting, while DTG is more challenging to determine. Direct DTG measurements usually require gas mass estimates from line detections (e.g., Vallini et al. 2018), which are often highly uncertain (e.g., Zanella et al. 2018; Salvestrini et al. 2025), or rely on knowledge of the ISM metallicity to exploit the DTG- Z_{gas} relation (e.g., Rémy-Ruyer et al. 2014; Popping & Péroux 2022; Algera et al. 2026).

We adopt a relation of the form:

$$\log \text{DTG} = A \log \left(\frac{T_{\text{dust}}}{\text{K}} \right) + B \log \left(\frac{\Sigma_{\text{SFR}}}{M_{\odot} \text{ yr}^{-1} \text{ kpc}^{-2}} \right) + C \log(1+z) + D \quad (6)$$

with $A = -4.129 \pm 0.027$, $B = 0.456 \pm 0.003$, $C = -1.295 \pm 0.019$, and $D = 4.521 \pm 0.042$. Comparing the DTG values predicted by this relation with the true values shows good, though not perfect, agreement ($R^2 \approx 0.78$), with a standard deviation of residuals of ≈ 0.2 dex. Although including additional variables or adopting more sophisticated – potentially machine-learning-based – parametrizations could improve performance, we opt for a simpler approach. This choice is motivated by the fact that large uncertainties in standard high- z gas conversion factors (e.g., Frias Castillo et al. 2025; Tripodi et al. 2024; Decarli & Díaz-Santos 2025) introduce errors comparable to, or greater than, those arising from the simple parametrization.

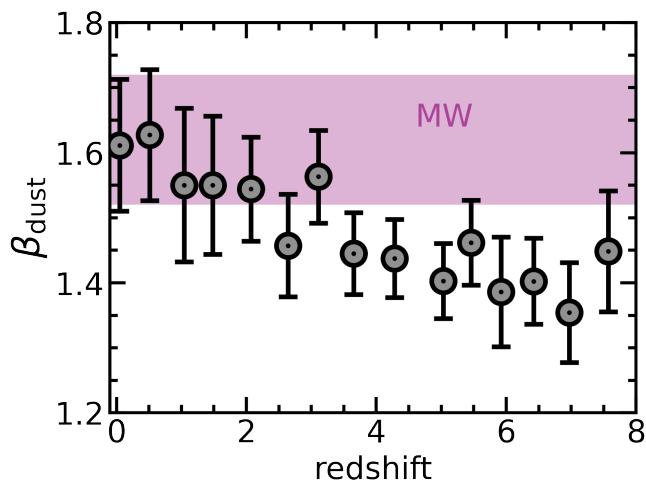


Fig. 7: Dust emissivity index evolution β_{dust} with redshift. Points and error-bars refer to median and 16 – 84th percentiles dispersion. The effective Milky Way value of $\beta_{\text{dust}} = 1.62 \pm 0.10$ is shown as reference as a purple area (Galliano et al. 2018).

3.4. Dust emissivity index

We present in Fig. 7 the redshift evolution of the dust emissivity index β_{dust} , which slightly increases down to low redshift. Owing to the strong anti-correlation between β_{dust} and T_{dust} in the SED fitting procedure, part of the observed redshift trend reflects the increase of T_{dust} with redshift discussed in Sect. 3.1. The dominant role of T_{dust} in driving variations of β_{dust} is further confirmed by a Shapley analysis analogous to that presented in Sect. 3.2, but with the emissivity index as the target variable (not shown here for brevity). In this case, T_{dust} is the most influential feature, with an importance more than a factor of $\gtrsim 3$ higher than that of any other parameter. At the same time, removing T_{dust} from the set of input features in the regression model reduces the test-sample coefficient of determination from 87% to 78%, highlighting once again the impact of the SED fitting-induced anti-correlation between these two quantities.

With this caveat in mind, we turn to a more physical speculation. Although β_{dust} is often linked to the chemical composition of dust grains, GRASIL adopts the classical grain absorption cross sections computed by Laor & Draine (1993), based on exact Mie theory for spherical grains. As a consequence, at wavelengths much larger than the grain size (typically longwards a few tens of microns and longer), the intrinsic emissivity index of individual grains is $\beta_{\text{dust}} = 2$.

Therefore, any deviation from this value does not arise from changes in the microscopic dust properties, but rather from the superposition of dust grains at different temperatures (e.g., Hunt et al. 2015). These temperatures depend on both the local radiation field and the grain size and composition. This temperature mixing flattens the far-IR decline of the SED, mimicking the effect of a lower emissivity index when the SED is fitted with a single-temperature MBB. The analysis in Sect. 3.2 suggests such a temperature mixing to be more pronounced at high redshift, where the contribution of warm molecular clouds is enhanced due to lower DTG ratios, resulting in a broader overall temperature distribution.

This point should also be kept in mind when interpreting values of β_{dust} (and T_{dust}) inferred under the simplifying assumption of a single dust temperature for the entire galaxy. Moreover, lab-

oratory measurements suggest that in real grains β_{dust} depends on, and in particular anti-correlates with, their temperature (e.g., Coupeaud et al. 2011).

Finally, we verified that adopting a fixed value of $\beta_{\text{dust}} = 1.6$, as measured in the Milky Way (Galliano et al. 2018) and consistent with the range commonly assumed in observational studies (e.g., see App. A), does not significantly impact the inferred evolution of dust temperature with redshift. The resulting T_{dust} values are fully consistent with the median trend shown in Fig. 3, showing an almost negligible difference up to $z < 2$ and only a modest reduction in the median T_{dust} at higher redshift ($\Delta T_{\text{dust}} \approx 4$ K).

4. Summary

In this paper, we have investigated the redshift evolution of dust temperature as predicted by a semi-analytic cosmological model of galaxy evolution that includes an explicit treatment of dust production and evolution (Parente et al. 2023), coupled with a radiative transfer pipeline to model the IR emission from dust grains (GRASIL; Silva et al. 1998). To reproduce as closely as possible the observational determination of dust temperature, we derive T_{dust} by fitting the resulting SEDs with a single-temperature MBB with the EOS-DUSTFIT code (Tripodi et al. 2024), under the optimistic assumption of full spectral coverage. Our main results can be summarized as follows.

- We find a clear increase in T_{dust} with redshift, in good agreement with the overall trend suggested by observational constraints, despite the large scatter present in the data.
- Using a Shapley analysis, we identify the star formation rate surface density Σ_{SFR} and the dust-to-gas (DTG) ratio as the primary drivers of the increase in T_{dust} toward high redshift, where galaxies host more compact and intense star formation and are more dust poor.
- The role of Σ_{SFR} can be understood in terms of higher star formation surface densities being associated with stronger radiation fields, leading to enhanced dust heating. Lower DTGs correspond to more optically thin molecular clouds – which appear hotter – and to a smaller number of dust grains over which stellar energy is distributed, resulting in increased heating per grain.
- The relations between T_{dust} and $\log \Sigma_{\text{SFR}}$ or \log DTG show a progressively steeper dependence with increasing redshift, which we parametrize with a broken power law. We also present a simple relation to derive DTG from Σ_{SFR} , T_{dust} , and redshift, which is particularly useful in observational studies where direct gas mass measurements are not feasible.

By combining, for the first time, a cosmological galaxy evolution model with explicit treatment of dust physics, detailed radiative transfer, and an observationally motivated strategy to infer T_{dust} , we have shown that the main drivers of warm dust temperatures in the early Universe are the star formation rate surface density and the DTG ratio. Early galaxies are generally more compact and optically thinner, which naturally leads to warmer dust. This finding, consistent with previous theoretical studies (e.g., Ma et al. 2019; Liang et al. 2019; Hirashita & Chiang 2022; Vijayan et al. 2022), is especially important for interpreting dust properties in high-redshift galaxies, where far-IR emission is often incompletely sampled.

It is nevertheless important to emphasize that the RT treatment adopted here – based on a two-phase ISM model consisting of diffuse gas and molecular clouds – is necessarily simplified due to the limited spatial resolution of the SAM. While this framework is made physically plausible (for example, by

including a finite escape time for young stellar populations from dense molecular clouds; [Silva et al. 1998](#)), it remains an oversimplification of the complex and irregular geometries of real galaxies. In our simulations, the gas component is imposed by construction to follow a disk-like configuration, a limitation that becomes particularly relevant at high redshift, where well-defined disk structures may not yet be in place (but see also [Ferreira et al. 2023](#); [Kartaltepe et al. 2023](#); [Sun et al. 2024](#)). Given the critical role of geometry in RT calculations, this constitutes a significant caveat of the model. A more realistic description would require full 3D hydrodynamic simulations, although producing large cosmological samples comparable to those generated by semi-analytic models remains challenging. A further point worth discussing concerns the observationally motivated derivation of T_{dust} . In this work, we have optimistically assumed the availability of full spectral coverage, a condition that is rarely met in real life. While this choice allows us to focus on the intrinsic predictions of the model and to maximize the robustness of the link between T_{dust} and galaxy physical properties, we note that sparse photometric coverage is often a major source of uncertainty in dust temperature estimates (e.g., [Casey 2012](#)). Moreover, current facilities do not allow observations of the rest-frame mid-IR emission of galaxies at $z \gtrsim 2$, where hot dust associated with star forming regions or AGN may dominate the SED, potentially revealing a different – and often suggested bimodal (e.g., [Liang et al. 2019](#)) – view of dust temperatures in galaxies. This underscores the importance of possible future facilities such as the *PRobe far-Infrared Mission for Astrophysics* (PRIMA; e.g., [Bradford et al. 2022](#)) in shedding new light on this topic.

Acknowledgements. MP was funded by NASA Astrophysics Theory Program grant 80NSSC24K1223 (PI: DN). FS and CF acknowledge financial support from the PRIN MUR 2022 2022TKPB2P - BIG-z, Ricerca Fondamentale INAF 2023 Data Analysis grant 1.05.23.03.04 “ARCHIE ARchive Cosmic HI & ISM Evolution”, Ricerca Fondamentale INAF 2024 under project 1.05.24.07.01 MINI-GRANTS RSN1 “ECHOS”, Bando Finanziamento ASI CI-UCO-DSR-2022-43 CUP:C93C25004260005 project “IBISCO: feedback and obscuration in local AGN”. DN is grateful for support from the NASA Astrophysics Theory Program via grants 80NSSC24K1223 and 80NSSC22K0716. GLG acknowledges financial support from the European Union’s HORIZON-MSCA-2021-SE-01 Research and Innovation Programme under the Marie Skłodowska-Curie grant agreement number 101086388 - Project LACEGAL.

References

Algera, H. S. B., Herrera-Camus, R., Aravena, M., et al. 2025, arXiv e-prints, arXiv:2512.02320

Algera, H. S. B., Inami, H., De Looze, I., et al. 2024a, MNRAS, 533, 3098

Algera, H. S. B., Inami, H., Oesch, P. A., et al. 2023, MNRAS, 518, 6142

Algera, H. S. B., Inami, H., Sommovigo, L., et al. 2024b, MNRAS, 527, 6867

Algera, H. S. B., Rowland, L., Stefanon, M., et al. 2026, MNRAS, 545, staf1897

Angulo, R. E. & Hilbert, S. 2015, Monthly Notices of the Royal Astronomical Society, 448, 364

Angulo, R. E. & White, S. D. M. 2010, Monthly Notices of the Royal Astronomical Society, 408, 1852

Aoyama, S., Hirashita, H., Lim, C.-F., et al. 2019, MNRAS, 484, 1852

Bakx, T. J. L. C., Algera, H. S. B., Venemans, B., et al. 2024a, MNRAS, 532, 2270

Bakx, T. J. L. C., Amvrosiadis, A., Bendo, G. J., et al. 2024b, MNRAS, 535, 1533

Bakx, T. J. L. C., Dannerbauer, H., Frayer, D., et al. 2020a, MNRAS, 496, 2372

Bakx, T. J. L. C., Sommovigo, L., Carniani, S., et al. 2021, MNRAS, 508, L58

Bakx, T. J. L. C., Sommovigo, L., Tamura, Y., et al. 2025, MNRAS, 544, 1502

Bakx, T. J. L. C., Tamura, Y., Hashimoto, T., et al. 2020b, MNRAS, 493, 4294

Beelen, A., Cox, P., Benford, D. J., et al. 2006, ApJ, 642, 694

Behrens, C., Pallottini, A., Ferrara, A., Gallerani, S., & Vallini, L. 2018, MNRAS, 477, 552

Bing, L., Oliver, S., Xiao, M., et al. 2025, arXiv e-prints, arXiv:2511.08672

Bischetti, M., Feruglio, C., Piconcelli, E., et al. 2021, A&A, 645, A33

Bischetti, M., Piconcelli, E., Feruglio, C., et al. 2018, A&A, 617, A82

Bradford, C., Glenn, J., Armus, L., et al. 2022, in American Astronomical Society Meeting Abstracts, Vol. 240, American Astronomical Society Meeting #240, 304.07

Camps, P. & Baes, M. 2015, Astronomy and Computing, 9, 20

Carniani, S., Gallerani, S., Vallini, L., et al. 2019, MNRAS, 489, 3939

Casey, C. M. 2012, MNRAS, 425, 3094

Chabrier, G. 2003, PASP, 115, 763

Clements, D. L., Pearson, C., Farrah, D., et al. 2018, MNRAS, 475, 2097

Costa, M., Decarli, R., Pozzi, F., et al. 2025, arXiv e-prints, arXiv:2512.03143

Coupeaud, A., Demyk, K., Meny, C., et al. 2011, A&A, 535, A124

da Cunha, E., Groves, B., Walter, F., et al. 2013, ApJ, 766, 13

Dale, D. A., Aniano, G., Engelbracht, C. W., et al. 2012, ApJ, 745, 95

Decarli, R. & Díaz-Santos, T. 2025, A&A Rev., 33, 4

Draine, B. T. 2003, ARA&A, 41, 241

Draine, B. T. & Lee, H. M. 1984, ApJ, 285, 89

Draine, B. T. & Li, A. 2007, ApJ, 657, 810

Dunne, L. & Eales, S. A. 2001, MNRAS, 327, 697

Duras, F., Bongiorno, A., Piconcelli, E., et al. 2017, A&A, 604, A67

Faisst, A. L., Fudamoto, Y., Oesch, P. A., et al. 2020, MNRAS, 498, 4192

Fernández Aranda, R., Díaz Santos, T., Hatziminaoglou, E., et al. 2025, A&A, 695, L15

Ferrara, A., Sommovigo, L., Dayal, P., et al. 2022, MNRAS, 512, 58

Ferreira, L., Conselice, C. J., Sazonova, E., et al. 2023, ApJ, 955, 94

Foreman-Mackey, D., Hogg, D. W., Lang, D., & Goodman, J. 2013, PASP, 125, 306

Franco, M., Elbaz, D., Zhou, L., et al. 2020, A&A, 643, A30

Frias Castillo, M., Rybak, M., Hodge, J. A., et al. 2025, ApJ, 987, 158

Galliano, F. 2018, MNRAS, 476, 1445

Galliano, F., Galametz, M., & Jones, A. P. 2018, ARA&A, 56, 673

Genzel, R., Tacconi, L. J., Lutz, D., et al. 2015, ApJ, 800, 20

Gilda, S., Lower, S., & Narayanan, D. 2021, ApJ, 916, 43

Granato, G. L., Lacey, C. G., Silva, L., et al. 2000, ApJ, 542, 710

Granato, G. L., Ragone-Figueroa, C., Taverna, A., et al. 2021, MNRAS, 503, 511

Gullberg, B., Smail, I., Swinbank, A. M., et al. 2019, MNRAS, 490, 4956

Guo, Q., White, S., Boylan-Kolchin, M., et al. 2011, MNRAS, 413, 101

Henriques, B. M. B., Yates, R. M., Fu, J., et al. 2020, MNRAS, 491, 5795

Hildebrand, R. H. 1983, QJRAS, 24, 267

Hirashita, H. & Chiang, I.-D. 2022, MNRAS, 516, 1612

Hodge, J. A., Swinbank, A. M., Simpson, J. M., et al. 2016, ApJ, 833, 103

Hogan, L., Rigopoulou, D., García-Burillo, S., et al. 2022, MNRAS, 512, 2371

Hopkins, P. F., Kereš, D., Oñorbe, J., et al. 2014, MNRAS, 445, 581

Hunt, L. K., Draine, B. T., Bianchi, S., et al. 2015, A&A, 576, A33

Jenkins, E. B. 2009, ApJ, 700, 1299

Kartaltepe, J. S., Rose, C., Vanderhoof, B. N., et al. 2023, ApJ, 946, L15

Kirkpatrick, A., Pope, A., Sajina, A., et al. 2015, ApJ, 814, 9

Kiyota, T., Ouchi, M., Iono, D., et al. 2026, arXiv e-prints, arXiv:2601.18149

Lamperti, I., Saintonge, A., De Looze, I., et al. 2019, MNRAS, 489, 4389

Laor, A. & Draine, B. T. 1993, ApJ, 402, 441

Liang, L., Feldmann, R., Kereš, D., et al. 2019, MNRAS, 489, 1397

Lim, C.-F., Wang, W.-H., Smail, I., et al. 2020, ApJ, 889, 80

Lower, S., Narayanan, D., Hu, C.-Y., & Privon, G. C. 2024, ApJ, 965, 123

Ma, X., Hayward, C. C., Casey, C. M., et al. 2019, MNRAS, 487, 1844

Magdis, G. E., Elbaz, D., Hwang, H. S., et al. 2010, MNRAS, 409, 22

Magdis, G. E., Rigopoulou, D., Hopwood, R., et al. 2014, ApJ, 796, 63

Magnelli, B., Lutz, D., Santini, P., et al. 2012, A&A, 539, A155

Mitsuhashi, I., Harikane, Y., Bauer, F. E., et al. 2024, ApJ, 971, 161

Narayanan, D., Conroy, C., Davé, R., Johnson, B. D., & Popping, G. 2018, ApJ, 869, 70

Narayanan, D., Torrey, P., Stark, D., et al. 2025, arXiv e-prints, arXiv:2509.18266

Nersesian, A., Xilouris, E. M., Bianchi, S., et al. 2019, A&A, 624, A80

Pallottini, A., Ferrara, A., Gallerani, S., et al. 2022, MNRAS, 513, 5621

Parente, M. 2025, arXiv e-prints, arXiv:2504.10585

Parente, M., Ragone-Figueroa, C., Granato, G. L., et al. 2022, MNRAS, 515, 2053

Parente, M., Ragone-Figueroa, C., Granato, G. L., & Lapi, A. 2023, MNRAS, 521, 6105

Parente, M., Ragone-Figueroa, C., Granato, G. L., et al. 2025, A&A, 697, A231

Planck Collaboration, Ade, P. A. R., Aghanim, N., et al. 2014, A&A, 571, A16

Popping, G. & Péroux, C. 2022, MNRAS, 513, 1531

Rémy-Ruyer, A., Madden, S. C., Galliano, F., et al. 2014, A&A, 563, A31

Renzini, A. & Peng, Y.-j. 2015, ApJ, 801, L29

Reuter, C., Vieira, J. D., Spilker, J. S., et al. 2020, ApJ, 902, 78

Salvestrini, F., Feruglio, C., Tripodi, R., et al. 2025, A&A, 695, A23

Santini, P., Maiolino, R., Magnelli, B., et al. 2014, A&A, 562, A30

Schaerer, D., Ginolfi, M., Béthermin, M., et al. 2020, A&A, 643, A3

Schreiber, C., Elbaz, D., Pannella, M., et al. 2018, A&A, 609, A30

- Scoville, N., Sheth, K., Aussel, H., et al. 2016, *ApJ*, 820, 83
- Shapley, L. S. 1953, 17. A Value for n-Person Games, ed. H. W. Kuhn & A. W. Tucker (Princeton: Princeton University Press), 307–318
- Shen, X., Vogelsberger, M., Nelson, D., et al. 2022, *MNRAS*, 510, 5560
- Silva, L., Granato, G. L., Bressan, A., & Danese, L. 1998, *ApJ*, 509, 103
- Simpson, J. M., Smail, I., Swinbank, A. M., et al. 2017, *ApJ*, 839, 58
- Sommovigo, L. & Algera, H. 2025, *MNRAS*, 540, 3693
- Sommovigo, L., Ferrara, A., Carniani, S., et al. 2022a, *MNRAS*, 517, 5930
- Sommovigo, L., Ferrara, A., Carniani, S., et al. 2021, *MNRAS*, 503, 4878
- Sommovigo, L., Ferrara, A., Pallottini, A., et al. 2022b, *MNRAS*, 513, 3122
- Springel, V., White, S. D. M., Jenkins, A., et al. 2005, *Nature*, 435, 629
- Sugahara, Y., Inoue, A. K., Hashimoto, T., et al. 2021, *ApJ*, 923, 5
- Sun, F., Wang, F., Yang, J., et al. 2025, *ApJ*, 980, 12
- Sun, W., Ho, L. C., Zhuang, M.-Y., et al. 2024, *ApJ*, 960, 104
- Traina, A., Gruppioni, C., Delvecchio, I., et al. 2024a, *A&A*, 681, A118
- Traina, A., Magnelli, B., Gruppioni, C., et al. 2024b, *A&A*, 690, A84
- Tripodi, R., Feruglio, C., Fiore, F., et al. 2024, *A&A*, 689, A220
- Tsukui, T., Wisnioski, E., Krumholz, M. R., & Battisti, A. 2023, *MNRAS*, 523, 4654
- Uematsu, R., Ueda, Y., Alexander, D. M., et al. 2025, *ApJ*, 979, 168
- Vallini, L., Pallottini, A., Ferrara, A., et al. 2018, *MNRAS*, 473, 271
- Viero, M. P., Sun, G., Chung, D. T., Moncelsi, L., & Condon, S. S. 2022, *MNRAS*, 516, L30
- Vijayan, A. P., Wilkins, S. M., Lovell, C. C., et al. 2022, *MNRAS*, 511, 4999
- Wakelam, V., Bron, E., Cazaux, S., et al. 2017, *Molecular Astrophysics*, 9, 1
- Witstok, J., Jones, G. C., Maiolino, R., Smit, R., & Schneider, R. 2023, *MNRAS*, 523, 3119
- Witstok, J., Smit, R., Maiolino, R., et al. 2022, *MNRAS*, 515, 1751
- Yang, M., Greve, T. R., Dowell, C. D., & Borys, C. 2007, *ApJ*, 660, 1198
- Younger, J. D., Omont, A., Fiolet, N., et al. 2009, *MNRAS*, 394, 1685
- Zanella, A., Daddi, E., Magdis, G., et al. 2018, *MNRAS*, 481, 1976

Appendix A: Observational data

In this section, we briefly summarize the properties of the observational samples included in Fig. 3 and discussed in Sect. 3.1. We compiled T_{dust} measurements from several literature studies spanning a wide range in redshift ($0 \lesssim z \lesssim 8.5$) and galaxy populations. For details about the selection criteria adopted and the analysis performed in each of the literature works, we refer to the references listed in this section.

We first consider works that report T_{dust} measurements for star forming galaxies, both in the local Universe (e.g., Clements et al. 2018; Lamperti et al. 2019; Nersesian et al. 2019; Sommovigo et al. 2021) and at higher redshift (e.g., Schreiber et al. 2018; Franco et al. 2020; Viero et al. 2022; Witstok et al. 2023). Most of the samples at intermediate and high redshift ($z > 1$) are dominated by dusty star forming galaxies and sub-millimetre galaxies (DSFGs and SMGs, respectively; e.g., Faisst et al. 2020; Bakx et al. 2021; Sommovigo et al. 2022a,b; Bing et al. 2025; Witstok et al. 2023), whose optical and UV emission is largely obscured by dust and whose bolometric output is predominantly emitted at far-IR and sub-millimetre wavelengths. The sample presented by Bakx et al. (2024a) instead consists of [C II]-emitting galaxies detected as companions of luminous quasars. In the highest redshift regime ($z \gtrsim 7$), the galaxies included in our compilation are predominantly classified as Lyman-break galaxies (e.g., Bakx et al. 2020b, 2025; Mitsuhashi et al. 2024; Sugahara et al. 2021; Witstok et al. 2022). Some of the considered samples also include galaxies whose observed brightness is significantly enhanced by gravitational lensing (e.g., Bakx et al. 2020a; Reuter et al. 2020).

We also included a few samples of ultra-luminous infrared galaxies (ULIRGs), mainly in the redshift range $0 \lesssim z \lesssim 2.5$ (e.g., Yang et al. 2007; Younger et al. 2009; Magdis et al. 2010, 2014). These systems are characterized by larger SFRs and Σ_{SFR} (e.g., Hogan et al. 2022), compared to galaxies lying on the star forming main sequence (e.g., Renzini & Peng 2015), and are therefore expected to exhibit higher T_{dust} as a consequence of their intense and compact star formation activity (e.g., Witstok et al. 2023).

Although our simulation does not explicitly include Active Galactic Nuclei (AGNs), we incorporated several observational samples of high-redshift AGN and QSOs (e.g., Duras et al. 2017; Bischetti et al. 2018, 2021; Tripodi et al. 2024; Costa et al. 2025; Fernández Aranda et al. 2025). AGN, and quasars in particular, can contribute significantly to dust heating even on kiloparsec scales (e.g., Tsukui et al. 2023; Fernández Aranda et al. 2025), potentially shifting the far-IR SED toward shorter wavelengths and yielding higher T_{dust} values when inferred using a single MBB. However, this effect does not appear to be systematic in the sources included in our compilation, suggesting that the combined contribution of AGN and stellar radiation to dust heating does not necessarily result in elevated T_{dust} values. We also note that the identification of AGN activity can be far from straightforward, especially in systems with relatively low AGN luminosities ($L_{\text{bol}} \approx 10^{43-44} \text{ erg s}^{-1}$) or in heavily obscured objects. As a result, some of the ULIRGs, DSFGs, and SMGs included in our compilation may host a dust-obscured AGN in their central regions (e.g., Uematsu et al. 2025; Kiyota et al. 2026).

Since we used a fit with a single-temperature MBB to derive T_{dust} , we preferred the works in the literature that fitted the far-IR SED with a single-temperature MBB. In the case of multiple methods adopted in a single study, we considered the T_{dust} measurements derived with a methodology similar to that adopted in Sect. 2.3. Some of the studies we included in Fig. 3 adopted a

fixed β_{dust} as they do not have enough photometric points in the Rayleigh–Jeans regime, to limit the degeneracy between β_{dust} and T_{dust} . In particular, the more common assumptions where $\beta_{\text{dust}} = 1.5$ (Younger et al. 2009; Magdis et al. 2010, 2014; Franco et al. 2020; Sugahara et al. 2021; Witstok et al. 2022; Bakx et al. 2024a; Mitsuhashi et al. 2024), $\beta_{\text{dust}} = 1.6$ (Duras et al. 2017), and $\beta_{\text{dust}} = 2$ (Bakx et al. 2020a, 2024b; Reuter et al. 2020). Franco et al. (2020) presented the results of the fit of the far-IR SED with a MBB on a sample of 35 galaxies at intermediate redshift, and discussed that when comparing the results obtained with $\beta_{\text{dust}} = 1.5$ and $\beta_{\text{dust}} = 2$, in the latter case T_{dust} values are ≈ 4 K lower, on average.

Sommovigo et al. (2021) introduced a new methodology that combined a single dust-continuum detection with the luminosity of [CII] at $158 \mu\text{m}$ emission line – a proxy of the gas mass – to constrain T_{dust} . The same methodology was then applied also to samples of high-redshift dusty star forming galaxies as those in the ALMA Large Program to INvestigate [CII] at Early times (ALPINE; Ferrara et al. 2022) and to the REBELS (Reionization Era Bright Emission Line Survey; Schaerer et al. 2020). The results were presented in Sommovigo et al. (2022a) and Sommovigo et al. (2022b), respectively. We checked the consistency of the [CII]-based approach with the single MBB model, and we found consistent results both for the sample of local galaxies (e.g., with the JINGLE and DustPedia samples; Lamperti et al. 2019; Nersesian et al. 2019, respectively) and for those at high- z (e.g., ALPINE; Faisst et al. 2020; Algera et al. 2024a,b, 2025).

Appendix B: T_{dust} dependence on additional galaxy properties

This appendix presents the same analysis shown in the main text for the two most influential properties affecting dust temperature (Σ_{SFR} and DTG) identified by the Shapley analysis (Sect. 3.2), but now applied to the other three key properties: specific SFR, molecular gas fraction, and depletion time (see Tab. 2).

Fig. B.1 shows the redshift evolution of T_{dust} as predicted by our model, binned according to these galaxy properties. Fig. B.2 illustrates the relations between dust temperature and these properties, along with their best-fitting broken power-laws (see Tab. 3).

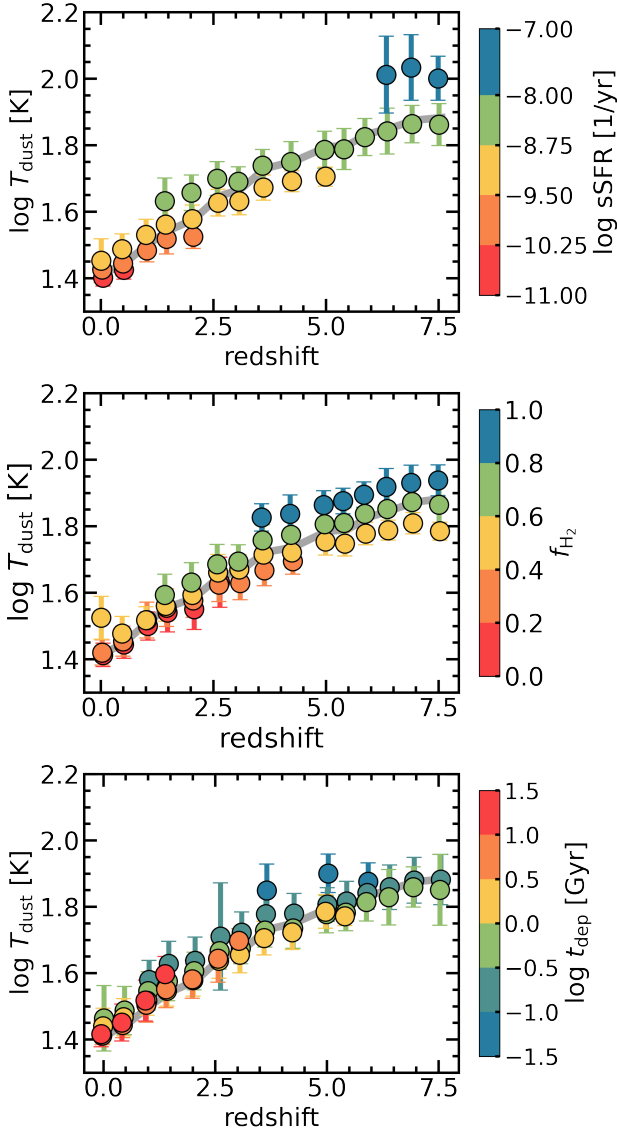


Fig. B.1: Dust temperature evolution with redshift separating galaxies in bins of specific SFR (top panel), molecular fraction (mid panel) and depletion time (bottom panel). Each panel shows the median and 16 – 84th percentiles of the distribution. Colors indicate bins in the corresponding property. The gray line in each panel refers to the full population.

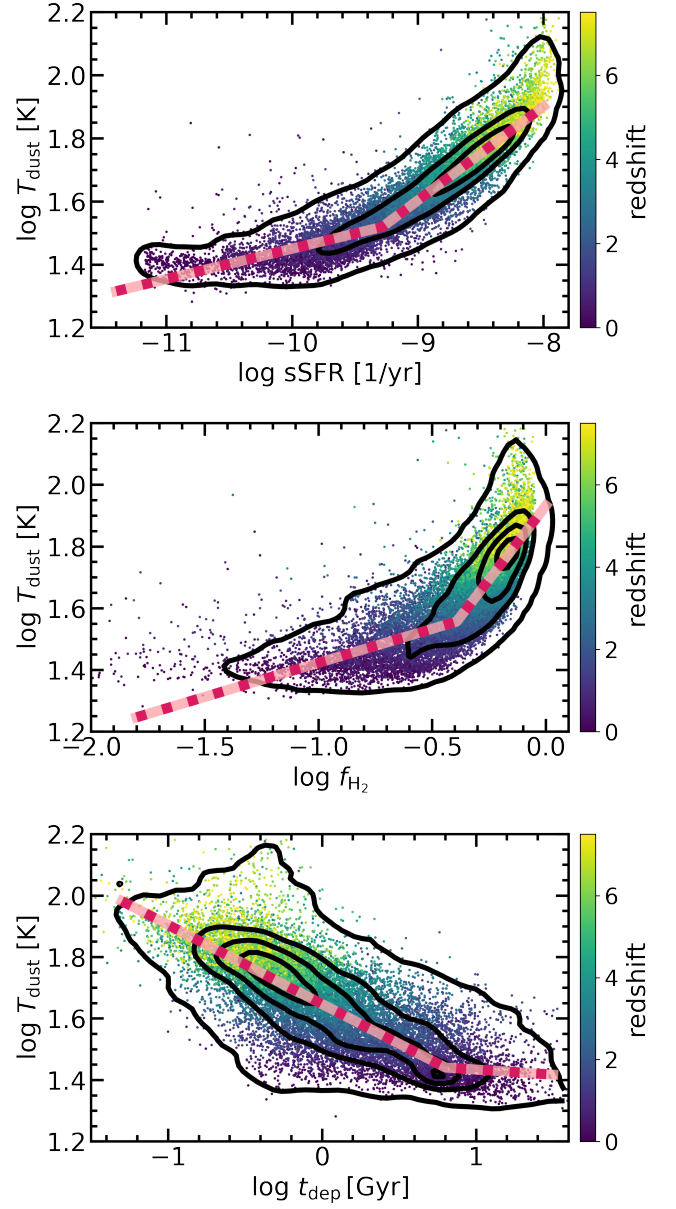


Fig. B.2: Dust temperature as a function of sSFR, molecular fraction f_{H_2} , and depletion time t_{dep} . Each point represents a galaxy and is color coded by redshift, while the black contours correspond to the full sample. The red dashed line shows a broken power law fit to data (Tab. 3).